Real-time through-thickness and in-plane strain measurement in Carbon Fibre Reinforced Polymer composites using planar optical Bragg gratings

Christopher Holmes[1], Mike Godfrey[2], Daniel John Bull[2], Janice Dulieu-Barton[3]
[1]University of Southampton, Optoelectronics Research Centre, Southampton, UK
[2]University of Southampton, School of Engineering, Southampton, UK
[3]University of Bristol, Bristol Composites Institute, School of Civil Aerospace and Mechanical Engineering, Bristol, UK

Abstract

A new strain sensor is proposed which can measure both through-thickness and in-plane strains within a laminated fibre-reinforced composite material. The planar sensor uses novel embedded planar optic sensors and is demonstrated on a carbon fibre composite test coupon. The planar optical sensor was fabricated via flame hydrolysis deposition and was physically machined to reduce the substrate thickness to <50 µm. Strain components are decoupled through monitoring the transverse electric and transverse magnetic effective refractive indices of two orthogonal planar waveguides. The work investigates if the embedded planar sensors have any mechanical knockdown effects on the composite structure and demonstrates their effectiveness at decoupling three orthogonal strain components.

1. Introduction

Measurement of through-thickness strains within advanced composites is an important parameter for structural health monitoring as they can provide an early indication for subsurface delamination between ply-layers. At present, no known sensor, including sensors in development, can achieve scalable strain measurements in the out-of-plane direction, i.e. through the thickness of the composite laminate. A solution that can measure through-thickness strain in real-time provides a means of better understanding of composite structural behaviour under unexpected loading configurations, manufacturing defects or impact events. Integrating such sensor capability into composite material provides a means of long-term structural health monitoring on high-value manufactured components such as wind turbines, or airframes.

At present, strain-monitoring approaches are generally split between electronic and optical methods. Electronic processes typically work on the principles of passing electrical current through materials to monitor electrical resistance and voltage changes that respond to strain changes caused by damage. The most common sensor in this category is the metal foil gauge. There have also been emerging developments to utilise novel conductive materials introduced into the composite, which work on similar principles. These materials include: conductive nano-particles introduced to the resin [1], piezoresistive nanotubes [2] and techniques which utilise the conductive carbon fibres [3], [4].

Unlike electronic monitoring techniques, optical methods have immunity to electromagnetic interference, permit monitoring over long-distance optical networks (several km) and present no spark risk. They typically utilise optical fibres embedded within the composite and are regarded as mature [5]–[7], with numerous developments made over the past several decades. Use of Fibre Bragg gratings (FBGs) is one of the most common approaches for discrete strain sensing. Other optical fibre monitoring approaches include utilise Rayleigh or Brillouin scattering principles, can permit fully distributed sensing along the length of an optical fibre, but typically have lower spatial resolution compared to FBGs. These methods typically infer the in-plane strains only, with no implementation yet demonstrated for through-thickness strain monitoring. Recent publications [8], have discussed theoretically the use of polarisation maintaining (PM) optical fibre as a means to resolve through-

thickness strain of a composite material [8]. However, the approach relies on consistent fast axis alignment, which for a cylindrical (or even D-shaped) optical fibre is very difficult to practically realise, due to the dynamic nature of the curing process and the optical fibre's potential for axial rotation.

The purpose of the current paper is to describe and demonstrate the development of flexible planar silica optical sensors where they can be embedded between layers in composite material with minimal mechanical compromise (i.e. knockdown) of structural performance. These new sensors sit under the classification of 'flexible integrated photonics', which generally refers to photonic devices fabricated upon flexible polymer [9], however recent work demonstrating flexible chalcogenides glass [9]–[13] and flexible silicon has been reported [14]. To the authors' knowledge, none of these flexible platforms have yet been embedded into a laminated polymer composite structure, and sensor polarisation has never been used to decouple composite strain components. Another important practical point to emphasise is that none of the above-mentioned solutions are based upon silica glass, rendering them less compatible for optical coupling to silica optical fibre and in turn for embedding as a sensor network within a composite structure. There have been some reports on utilising flexible planar silica optical fibre as a sensor[15], [16] but so far demonstration of its inherent strain response has been elusive.

In this paper, a unique ultra-thin silica planar optical sensor is positioned between the ply layers of carbon fibre reinforced polymer (CFRP), to simultaneously decouple in-plane and through-thickness strain components. Whilst the strain response of silica-based planar optics has been documented [17], [18], this has so far been limited to optical micromechanical structures. It has not yet been used to map strain within a composite structure. To the authors' knowledge, this is the first reported demonstration of embedded planar optics in CRFP. The approach is scalable, and the work described here provides an important first step to achieving real-time, through-thickness and in-plane strain monitoring. Furthermore, the optical functionality associated with planar optics potentially enables multiplexing and demultiplexing of optical signals and optical switching capability in future development [19].

2. Concept and Theory

The proposed decoupling of strain components works on the principle that TE (transverse electric) and TM (transverse magnetic) optical polarisations can travel at different speeds (observe different refractive indices, n) depending upon the strain a body is subjected to. If this is measured using planar Bragg gratings, the spectral responses $\Delta\lambda$ are influenced by the linear strain components, ε_x, ε_y and ε_z, along the x, y and z directions respectively, defined as [20]:

$$\frac{\Delta\lambda_x}{\lambda_x} = \varepsilon_y - \frac{n_x^2}{2}\Big(p_{11}\varepsilon_x + p_{12}\big(\varepsilon_y + \varepsilon_z\big)\Big) + \eta_x \Delta T \tag{1}$$

$$\frac{\Delta\lambda_z}{\lambda_z} = \varepsilon_y - \frac{n_z^2}{2}\Big(p_{11}\varepsilon_z + p_{12}\big(\varepsilon_y + \varepsilon_x\big)\Big) + \eta_z \Delta T \tag{2}$$

where the first term relates to a physical length change in grating pitch, the second term is the strain-optic response dependent upon the Pockels coefficients p_{11} and p_{12} and the third term is the thermal response dependent upon the thermo-optic constant η and change in temperature ΔT. The Pockels coefficients, p_{11} and p_{12} are 0.121 and 0.270 respectively for fused silica [21], with recent work estimating values for SMF-28 optical fibre to be closer to 0.116 and 0.255 respectively (at a wavelength 1531 nm) [22]. The subscripts in Equations (1) and (2) denote Cartesian coordinates with y being the

modal propagation direction. Nomenclature for wavelength and refractive index subscripts relate to the respective alignment of the electric field in space, that is to say, TE or TM polarisation.

The work in the present paper considers planar waveguides that are embedded within a composite laminate, as illustrated in Figure 1. In this arrangement, decoupling of strain components can be made by noting the inherent alignment of the TE and TM modes to the composite geometry.

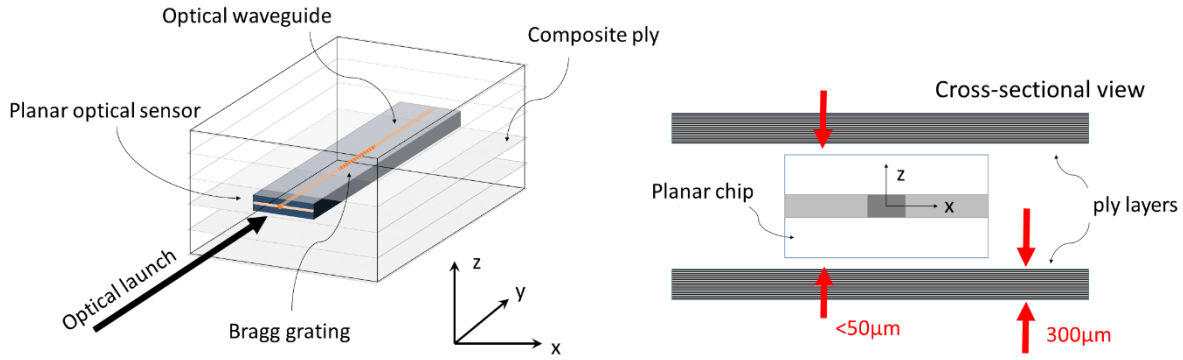

Figure 1 A cross-sectional view of a planar waveguide (not to scale).

From Equations (1) and (2) it can be seen that the change in spectral birefringence of the planar waveguide is dominated by the second term. Assuming the thermo-optic response and effective refractive indices are comparable for both polarisations, the difference in birefringence can be approximated by

$$(\Delta\lambda_x - \Delta\lambda_z) \approx \gamma(\varepsilon_x - \varepsilon_z) \tag{3}$$

where $\boldsymbol{\gamma}$ is a constant, dependent upon the photoelastic parameters of the waveguide, for the glass platform considered in this work the value is positive. For a single planar Bragg grating, as illustrated in Figure 1 the strain difference between the through-thickness, ε_z, and orthogonal in-plane strain component ε_x can be inferred through the change in birefringence. All three linear strain components can be decoupled through use of two orthogonally aligned planar waveguides and monitoring the TE and TM polarisations in each respectively. This would result in a set of four simultaneous equations with four unknown terms, three strain components and temperature component expressed as follows:

$$\begin{pmatrix} V_{TE} \\ V_{TM} \\ H_{TE} \\ H_{TM} \end{pmatrix} = \begin{bmatrix} -\frac{n^2}{2}p_{11} & \left(1-\frac{n^2}{2}p_{12}\right) & -\frac{n^2}{2}p_{12} & \eta_{V_{TE}} \\ -\frac{n^2}{2}p_{12} & \left(1-\frac{n^2}{2}p_{12}\right) & -\frac{n^2}{2}p_{11} & \eta_{V_{TM}} \\ \left(1-\frac{n^2}{2}p_{12}\right) & -\frac{n^2}{2}p_{11} & -\frac{n^2}{2}p_{12} & \eta_{H_{TE}} \\ \left(1-\frac{n^2}{2}p_{12}\right) & -\frac{n^2}{2}p_{12} & -\frac{n^2}{2}p_{11} & \eta_{H_{TM}} \end{bmatrix} \begin{pmatrix} \varepsilon_x \\ \varepsilon_y \\ \varepsilon_z \\ \Delta T \end{pmatrix} \tag{4}$$

where *V* and *H* correspond to the normalised spectral response, *Δλ/λ*, for light propagating in waveguides aligned to the *y-axis* and *x-axis* respectively. It can be assumed that the TE and TM effective refractive indices are comparable, for the waveguides aligned along the y-axis (i.e. n_x and n_z)

and x-axis (i.e. n_y' and n_z') respectively. That is to say $n \approx n_x \approx n_z \approx n_y' \approx n_z'$. Through use of equation 4, it is possible to decouple linear strain and temperature.

3. Manufacturing procedure and integration of sensors

3.1 Planar Sensor Fabrication

Planar chip fabrication was conducted using Flame Hydrolysis Deposition (FHD), which feeds chloride-based precursors through an oxy-hydrogen flame. FHD deposits a silica-based soot onto a substrate, which is subsequently consolidated at high temperatures. The FHD recipes used for sensor fabrication are outlined in Table 1. They began with a 1 mm thick, 6-inch diameter silicon wafer of orientation (100), with a 6 µm layer of thermally grown oxide. The oxide was grown in a wet furnace, which acted as a buffer layer between the FHD and silicon. In total three FHD layers were deposited and subsequently consolidated.

Layer	H_2:0_2 l/min	$SiCl_4$ (sccm)	$GeCl_4$ (sccm)	BCl_3 (sccm)	PCL_3 (sccm)	Consolidation temperature	Thickness	Refractive index *
1	6.5:1.5	137	0	70	31	1250 °C	31 µm	1.4452
2	5.4:2.7	123	130	16	0	1360 °C	5 µm	1.4635
3	6.5:1.5	137	0	70	31	1250 °C	16 µm	1.4452

Table 1 the fabrication detail used (*at 1553nm wavelength).

The thickness of the underclad (layer 1) was purposefully made thicker than the overclad (layer 3) as the silicon substrate was removed through mechanical processing. This thick underclad permitted a thickness of sacrificial glass to be present, ensuring the evanescent field of the waveguide mode was not exposed after the silicon removal process. To define the planar waveguides and Bragg gratings, a dual beam direct UV writing process was used [23], with a writing fluence of 14kJcm^{-2}. Prior to UV writing the planar substrate was hydrogenated at 120 bar for 10 days. The thickness of the planar optical sensor was reduced to minimise the mechanical influence it had on the composite. Silicon and part of the FHD underclad was removed through the use of a Loadpoint MicroAce dicing saw and a synthetic diamond impregnated resin blade (DISCO R07-SD400 series). The bulk silicon was removed using a rastering sequence. The kerf of the blade was 250 µm, raster pitch of 90 µm, a feed rate of 5 mms^{-1} and spindle speed of 25,000 RPM. The resulting surface quality had <3 µm waviness. It was noted that machining down to the silica in one cut generated a large force, which resulted in the sensors debonding from the dicing tape. Therefore, machining was performed with two passes. A high-tack dicing tape was avoided to reduce the risk of cracking the sensor when transferring to the composite. The tape used (LP000579) was UV exposed for 30 minutes to soften the adhesive, enabling good sensor transfer.

3.2 Planar sensor integration into composite material

Planar sensors were placed within the composite layers (XPREG® XC130 epoxy-based unidirectional carbon fibre prepreg) during ply layup. The sensors were attached to a dicing backing tape which helped with the handling and positioning of the sensors onto the uncured prepreg surface. Once placed into position, the dicing tape was removed. During layup, the position of each sensor was measured with respect to two reference edges. The composite was then vacuum bagged and consolidated under vacuum for 10 minutes. An autoclave process was used to cure the panel under vacuum at 5 bar gauge pressure throughout both the cure and post-cure processes which were conducted at 120 °C for 1 hour and 130 °C for 2 hours respectively. After curing, the position of the sensors was measured with respect to the same two reference edges measured from during layup.

Expansion of the laminate during the curing process was accounted for. The specimens were cut oversize with a tile saw before grinding to final size using 120 grit silicon carbide grinding paper. Sensors that protruded towards the free-edge of the composite were trimmed with a dicing saw so that the sensors could be optically coupled with optical fibre. The cross-section of an embedded sensor is shown in the micrograph in Figure 2.

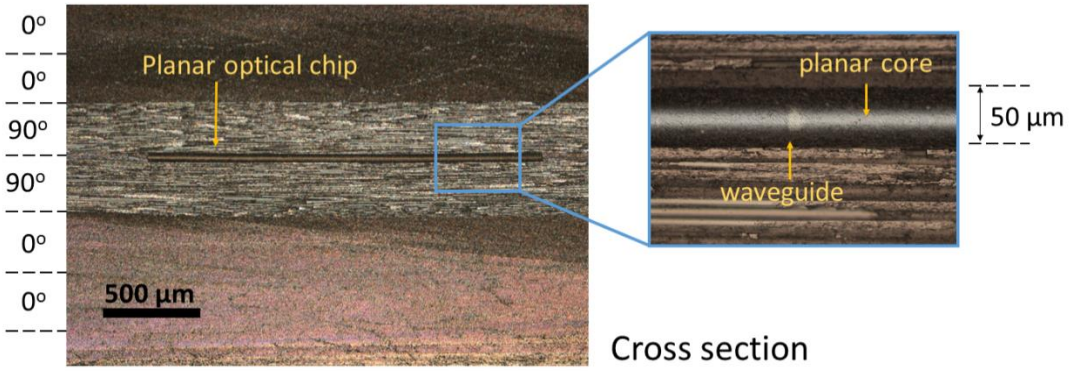

Figure 2 Cross-sectional micrograph of an integrated optical chip embedded centrally in carbon fibre reinforced polymer $[0/0/90]_s$. The planar silica chip is 50 µm thick and back illuminated with white light to observe waveguide and planar core layer.

4. Mechanical Integrity

One of the key challenges with embedding sensors is minimising their impact on the structural performance of the laminated composite material. Therefore, it was decided to assess the potential structural knockdown using short beam shear (SBS) tests to assess any changes in the interlaminar shear strength resulting from the presence of the planar sensors. As a baseline, a comparison was made for the instance of no sensor present and additionally, for comparison with existing optical fibre technology, tests were performed on embedded polyimide coated optical fibre.

4.1. Short Beam Shear test specimen preparation

Silica planar optic blanks ("dummy" sensors) 5 mm wide, 10 mm long by ~50 µm thick were embedded between the central plies (plies 4 and 5) during layup. Two types of CFRP (carbon fibre reinforced polymer) stacking were tested for SBS, each of which were made into plates measuring 300 mm square by 2 mm thick. The first plate had a unidirectional 8 ply layup $[0]_8$ and the second had the layup $[0/0/0/90]_s$. In both instances, the silica blanks were placed between the central plies of the composite layup. The SBS test series is provided in Table 2 and investigated 80 µm diameter optical fibre (with an 11.6 µm thick polyimide coating, 103.1 µm total diameter).

Specimen type	Embedded sensor blank type	Layup	Number of repeats	Notes
#1	No sensor	$[0]_8$, $[0/0/0/90]_s$	8	Comparison
#2	Silica planar sensor	$[0]_8$, $[0/0/0/90]_s$	8	New sensor
#3	Polyimide coated optical fibre (103.1 µm diameter)	$[0]_8$, $[0/0/0/90]_s$	3	Comparison

Table 2 Initial specimen and test information for short beam shear test.

4.1. Short beam shear tests

SBS tests were performed on an Instron 5569 electromechanical test machine and consisted of a 3-point bend test with a roller separation of 10 mm to promote failure from internal shear, rather than bending failure (see figure 3). The experimental method was performed in accordance with EN 2563.

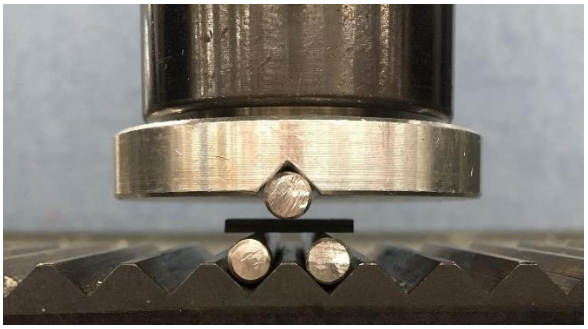

Figure 3 Short beam shear test experimental arrangement.

CFRP specimens were cut and ground to within ±0.1 mm of the nominal dimensions (20 mm by 15 mm by 2 mm thick). The specimen dimensions were in accordance with EN 2563, with one modification: the specimen width was made 5 mm wider than the standard to ensure each sensor was fully contained within the specimen. As all specimens were of identical size any impact on the results would be consistent throughout the test series, which was understood to be acceptable for the purposes of the comparative study.

SBS tests were initially conducted on test coupons containing no sensors (#1), an embedded normal planar sensor (#2) and an 80 µm diameter optical fibre with polyimide coating (#3). Upon conducting the initial tests, X-ray computed tomography (CT) scans were carried out to capture the damage mechanisms and interactions between the sensor and composite material. In comparison to embedded optical fibre Figure 4 (c) - (d), the embedded planar optical sensor Figure 4 (a) - (b) can be observed to have an identical damage mode (shear crack). The images further reveal delamination damage and cracks generating from the corners of the sensor as shown in Figure 4 (a) and cracks occurring through the sensor, shown in Figure 4 (b).

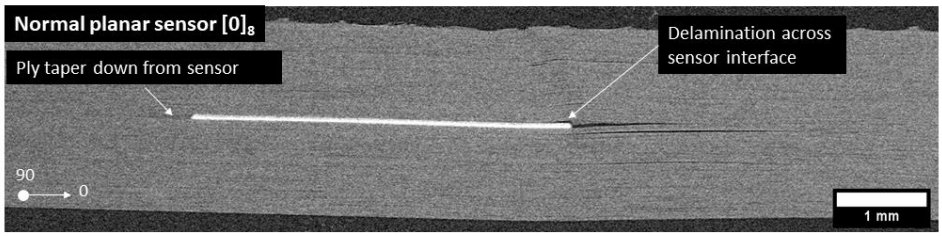

(a)

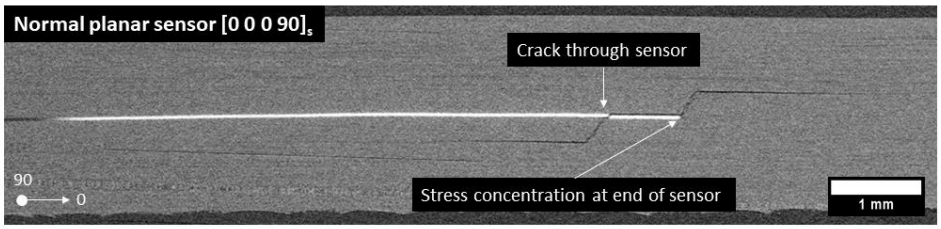

(b)

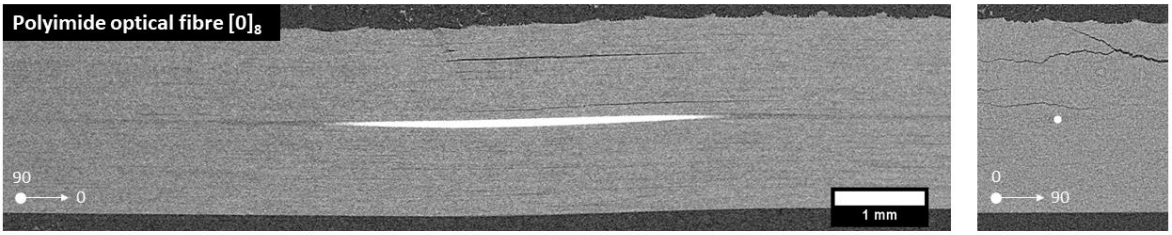

(c)

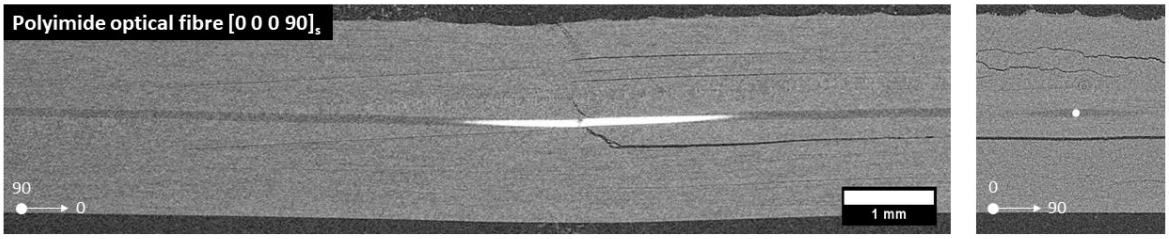

(d)

Figure 4 X-ray CT cross-sections showing two modes of failure for the planar optical sensors (a) delamination across the sensor surface and (b) crack penetration through sensor, observed after short shear beam tests were conducted to failure. Comparison is made to failure modes of embedded optical fibre (c) $[0]_8$ layup and (d) $[0\ 0\ 0\ 90]_s$ layup.

The X-ray CT images (Figure 4) and optical micrograph images (Figure 2) both indicate inherent ply tapering at sensor edges, which present epoxy rich regions. Further to this, the X-ray CT scans also revealed delamination occurring preferentially on the smooth side of the sensor, i.e. the overclad side where the silicon substrate was not removed by machining. In Figure 4 it is clearly evident that cracks developed from the sharp end of the sensor where a stress concentration exists. In the light of the results shown in Figure 4, a decision was made to improve the interfacial bond strength between the plies and sensor by surface roughing, and to reduce the stress concentrations at the corners of the sensors by tapering the planar chip edges. These modifications are included in the test series given in Table 3, which were used to investigate the inclusion of the feature in $[0]_8$ specimens only.

Design feature	Specimen type / Variant		Number of Repeats	Detail
Roughened Dual-side	**#4**	Planar sensor with both sides roughened with dicing saw	4	This sensor was 3.5 µm thinner than the normal planar sensor.
	#5	Smooth side roughened with a Hydrofluoric acid etch.	5	This sensor was 2 µm thinner than the normal planar sensor.
Tapered edge	**#6**	Planar sensor with edges tapered in dicing saw	3	Attempt to increase the interfacial bonding strength
	#7	Planar sensor with edges tapered by an HF etch	5	Significant breakage during embedding process
Thinner	**#8**	Thinning the planar sensor to ~30 µm	2	Difficult to manufacture without cracking

Table 3 Fabrication strategies tested to reduce the influence of the sensor on the structural performance of the laminated composite $[0]_8$ only

Figure 5 (a) and (b) indicate representative load-displacement curves for the specimens listed in Table 2. It should be noted that there is little difference between the control specimen and that with the embedded sensor. However, there is a sharper reduction in load $[0/0/0/90]_s$ compared to a more progressive failure on the $[0]_8$, which is considered to be a function of the different material lay-up and not attributed to any effect of the sensor. Figure 5 (c)shows the maximum mechanical loads at which the test coupons, described in Tables 2 and 3, failed. It is clear that for the $[0]_8$ system, the non-processed sensors have a slight detrimental effect on the interlaminar shear strength. It can be observed that in general, processing the sensors either by roughening the planar surface or tapering the edges has reduced the sensor's impact on the performance of the laminated composite material. Further reducing the sensor thickness to 30 µm also presents a possible improvement in the structural integrity but presents notable manufacturing and handling difficulties. The polyimide coated silica optical fibre and some post-processed planar sensors embedded in the $[0]_8$ system showed larger average maximum load values than the case of no sensor coupon. However, it should be noted that these measurements sit within one standard deviation spread of respective data sets and therefore due to this variation not believed to be statistically significant. Figure 4 indicates that the embedded optical fibre, in the $[0\ 0\ 0\ 90]_s$ system, creates local fibre waviness which likely contributes towards the slightly smaller failure stress observed in Figure 5.

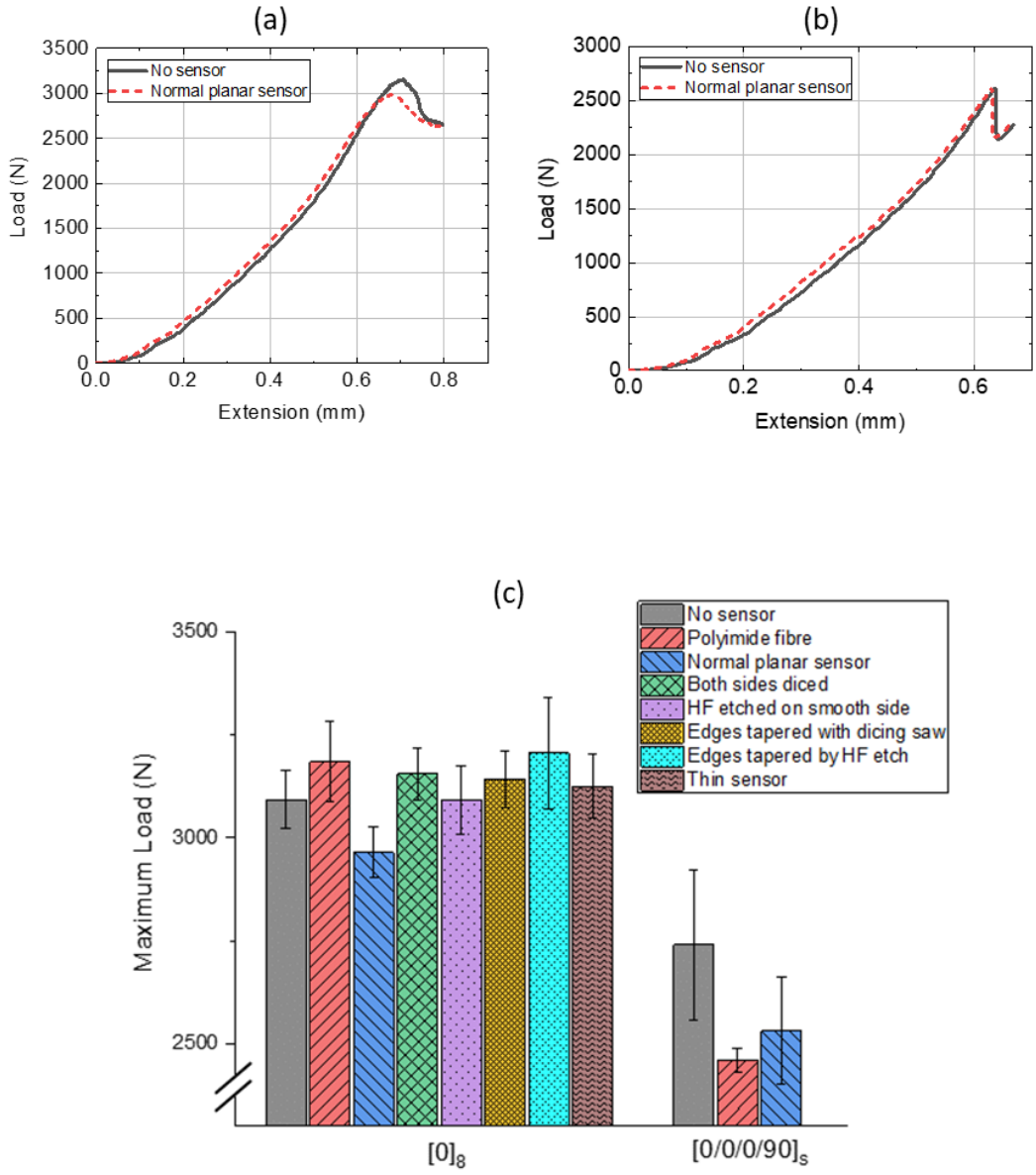

Figure 5 Representative load-displacement curves for no sensor, planar sensor and polyimide coated sensor for (a) $[0]_8$ (b) $[0/0/0/90]_s$ and (c) a bar chart showing the maximum load reached by each sample in a short beam shear test. Error bars: ±1σ of the repeated measurements.

5. Optical Sensitivity

To quantify the optical performance of the embedded sensors, tensile strain and thermal response experiments were conducted. The component under test was a coupon of carbon fibre composite, depicted in Figure 6, with two sensor chips located in the central layers of the composite. The chips labelled as horizontal and vertical contained a single straight waveguide that ran the length of the chip, i.e. with reference to Figure 6 (b), the horizontal sensor guided light along the x-axis and the vertical sensor guided light along the y-axis. To increase sensitivity with applied load and limit the clamping force of test machine grips the layup was reduced from 8 ply to 4 ply, configured [0/90]s.

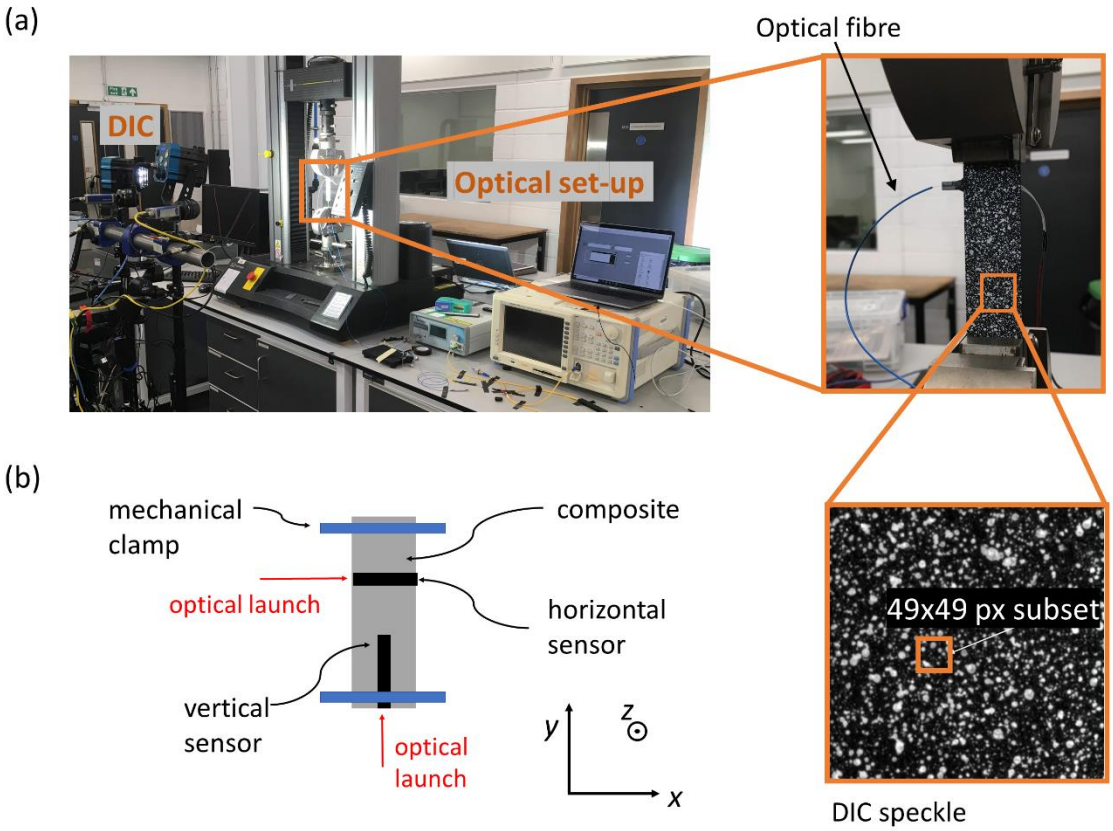

Figure 6 Experimental arrangement for optical performance showing (a) photograph set-up and (b) schematic depicting the positioning of the optical planar sensors within the composite test piece. In this arrangement the loading direction is parallel to the y-axis.

The planar chips were fabricated using a direct UV laser writing process, which can simultaneously define Bragg gratings and waveguides in a single-step process. The writing conditions for each chip were identical. Both writing steps were written at a laser fluence of 14 kJcm^{-2} and contained four Gaussian apodised Bragg gratings with a duty cycle of 0.8 and grating length of 12 mm. The planar Bragg gratings were defined end-to-end and thus collectively covered a 48 mm length. Through a detuning technique, the gratings were defined at 50 nm spectral separation permitting multiplexing.

5.1. Mechanical loading: optical strain measurement response

Mechanical quasi-static tensile tests were conducted within the linear elastic range of the composite. The specimen had a $[0/90]_s$ layup and the sensors were placed centrally within the thickness of the laminate. Strain signals from the optical sensors were compared with strain measurements obtained using electrical foil strain gauges, and digital image correlation (DIC).

The optical arrangement used a 5 element superluminescent LED broadband light source (Amonics ASLD-CWDM-5-B-FA) and an Optical Spectrum Analyser (OSA) (Ando AQ6317B). Light was coupled into the optical sensor using a v-groove fibre PM pigtail, which was attached to the side of the composite using UV cured optical epoxy (Dymax OP-4-20641). A 3 dB coupler and PM polariser delivered the light to the sensor and returned it to the OSA. Measurements switched between TE and TM polarisations for the two respective embedded sensor elements.

From Figure 7 it can be observed that the waveguides are multimode, as Bragg reflection consists of a fundamental and a series of higher order mode peaks. This was a result of the underclad FHD layer

(layer 1) having a consolidation temperature lower than the core layer above. It is considered that this resulted in diffusion of the Germanium dopants into the clad layers, increasing the effective waveguide thickness. The proof-of-concept demonstration is not affected by the waveguide thickness and in the future could be reduced to a single mode structure by layer optimisation resulting in improvements in the sensor's multiplexing capability.

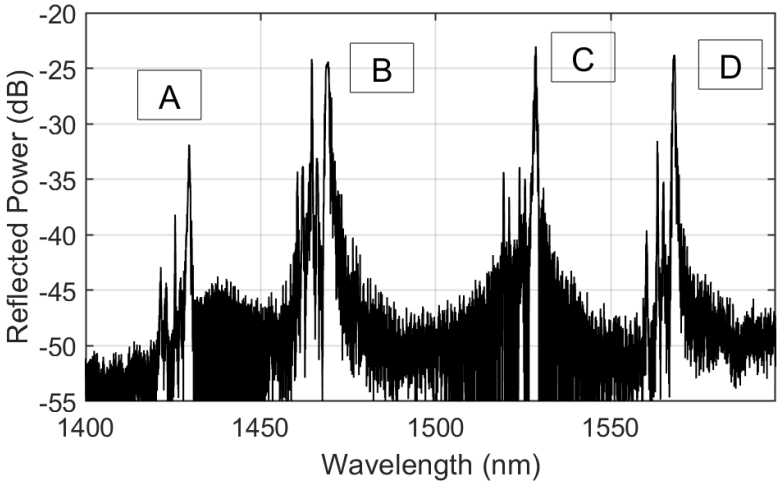

Figure 7 Spectral back reflection of direct UV written Bragg gratings embedded into the planar chip.

For data collection, the second order modes were taken, as the first order modes had a saturated grating response (100% reflectivity leading to flat top response). By using the second order mode, the precision of the spectral fit was enhanced by approximately a factor of 5.

The average effective refractive index for the horizontal sensor was 1.4574 (first order mode) and 1.4546 (second order mode). For the vertical sensor, values were 1.4576 and 1.4551 respectively. It should be noted that this assumes the period of the Bragg grating is unaltered after writing. However, the removal of silica from the silicon substrate and additional effects caused by the embedding process and material curing may change the period of the Bragg grating. For the purpose of the proof-of-concept, it is assumed this has only a small influence but will become the subject of further investigative work.

In carrying out the experiments, the specimen was loaded in-plane at incremental displacement steps using an electromechanical test machine operated in displacement control. The specimen dimensions were as follows: ungripped length = 108 mm; specimen width = 36 mm; average thickness = 1.10 mm. Strain gauges were bonded to the specimen surface, in the same position and orientation as the optical sensors.

For each reading, the test machine (Instron 5569 electromechanical test machine) was programmed to increment the crosshead upwards (to generate a tensile load on the specimen) at a rate of 1 mm/min in 10 µm intervals for the first 10 readings. The interval was increased to 30 µm for the remaining three readings. The crosshead remained stationary while data from the optical sensors was collected. This involved scanning both sensors independently in both TM and TE polarisations. Mean values from the strain gauges were taken during the optical measurement period. The experiment was stopped when the strain gauge readings drifted in excess of ±5% about the mean value. A third strain measurement technique: stereo digital image correlation (DIC) was also conducted for comparison.

Figure 8 shows the spectral response of the Bragg gratings subject to electromechanical actuation. The vertical sensor indicates the largest spectral response with applied force. This can be understood from Equation (1), which has a dominant first term related to strain along the direction of light propagation. For the vertical sensor, this is along the y-axis, so the response is as expected. The positive trend indicates the sensor is under tensile strain along the y-axis, as expected. The horizontal sensor has light propagating along the x-axis. The smaller negative gradients indicate compressive strain along the x-axis, which is smaller in magnitude than the strain in the z-axis, also as expected.

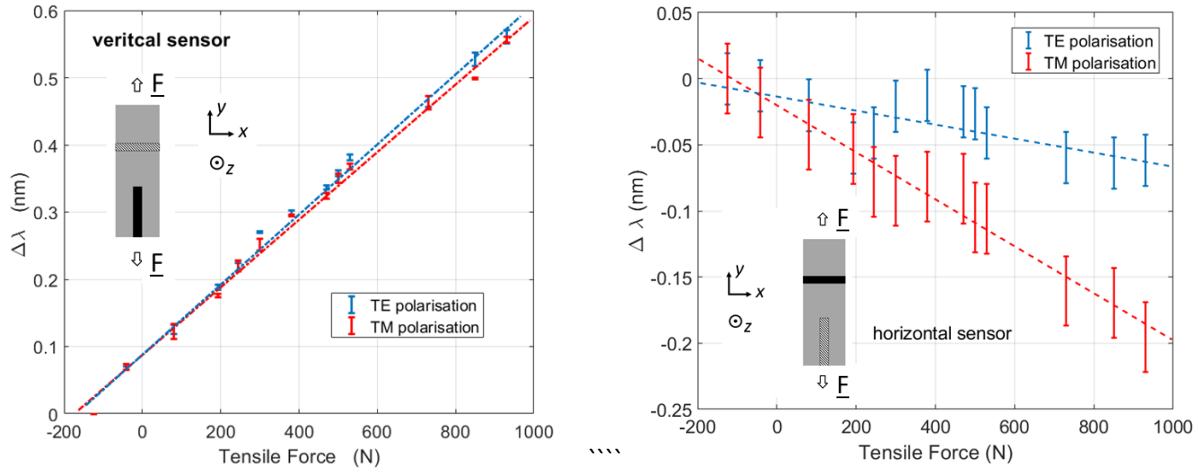

(a) (b)

Figure 8 The TE and TM response of the planar Bragg grating sensors in (a) the vertical and (b) the horizontal orientation with respect to the tensile load.

As the strain components along the *x-axis* and *z-axis* (through-thickness) are under compression, for $(\Delta\lambda_{TE} - \Delta\lambda_{TM})$ to be positive for the vertical sensor, the magnitude of through-thickness strain must be greater than that of the in-plane strain (i.e. $|\varepsilon_z| > |\varepsilon_x|$), understood from Equation (3). Therefore, from graphical inspection, it can be inferred that $|\varepsilon_y| > |\varepsilon_z| > |\varepsilon_x|$, as expected.

Symbol	Detail	d(Δλ/λ₀) / dF (N⁻¹)	Error
V_{TE}	Vertical sensor TE	3.493×10^{-7}	0.01 %
V_{TM}	Vertical sensor TM	3.413×10^{-7}	0.6 %
H_{TE}	Horizontal sensor TE	-3.396×10^{-8}	18 %
H_{TM}	Horizontal sensor TM	-1.117×10^{-7}	6 %

Table 4 Summary of the spectral response, subject to tensile strain

Table 4 summarises the spectral responses (gradients) observed in Figure 8. Note, the response in each case is normalised to the initial wavelength, i.e. is representative of the values on the left-hand side of Equation (4). The strain components presented in Section 5.3 were calculated using this data set, Equation (4) and use of the Nelder-Mead method with weighted fitting. The remaining parameter to quantify in Equation (4) is the thermo-optic response.

5.2 Thermo-Optic Response

The thermo-optic response was characterised by placing the horizontal and vertical sensor upon a Peltier bed (Deben Peltier cool stage). Optical characterisation was made at four separate temperature values and the response of grating number 3 is shown in Figure 13 for each polarisation of both horizontal and vertical sensors.

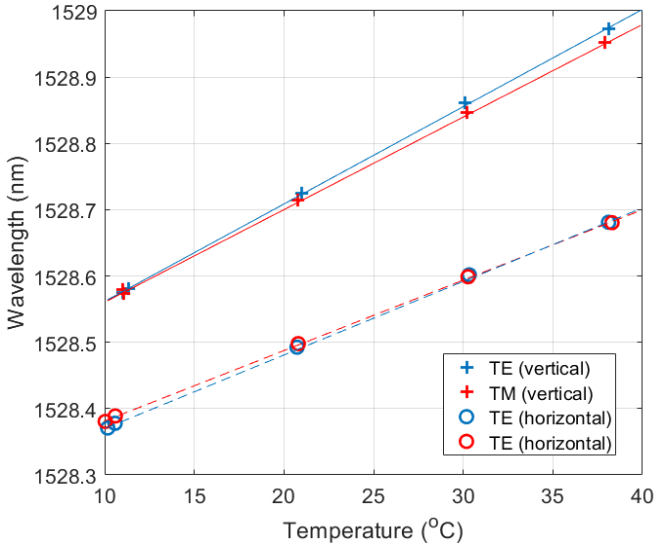

Figure 9 Thermo-optic response of the TE and TM mode in horizontal and vertical orientation.

It is noted that an offset of ~200 pm is present between the horizontal and vertical sensor, corresponding to a $1x10^{-4}$ effective refractive index difference. This could feasibly be the result of variation in the deposited glass thickness and refractive index, laser power fluctuations and out-gassing of hydrogen during the UV writing process or strain asymmetry during the curing process.

Symbol	Detail	Thermo-optic response (pm/K)
$\eta_{V\_TE} .\lambda_{V\_TE}$	vertical TE	14.7 ± 0.1
$\eta_{V\_TM} .\lambda_{V\_TM}$	vertical TM	14.0 ± 0.1
$\eta_{H\_TE} .\lambda_{H\_TE}$	horizontal TE	11.2 ± 0.1
$\eta_{H\_TM} .\lambda_{H\_TM}$	horizontal TM	10.6 ± 0.1

Table 4 summary of thermo-optic response

From Table 4 a relative difference between the thermo-optic responses of 3 pm/K is observed, with the vertical orientated sensors showing the greatest thermal response.

5.3 Strain Measurement

To show the strain measurement capability of the optical planar sensors, direct comparisons were made using the strains obtained from an electrical strain gauge and from DIC at a tensile load of 1 kN. The electrical strain gauges (supplied by Omega, model KFH-03-120-C1-11L1M2R), had resistance of 120.4 Ω ± 0.35%, gauge factor of 2.07 ± 1.0%, transverse sensitivity of -0.1% and thermal expansion coefficient of $10.8x10^{-6} K^{-1}$. Stereo DIC was used to account for out-of-plane displacement of the specimen. To prepare specimens for DIC, specimens were first painted with a base coat of matt black spray paint, followed by the application of a speckle pattern using white matt paint. Stereo DIC images were acquired using two 5 megapixel E Lite CCD cameras with 50 mm Nikkor lenses. Image magnification was achieved by adjusting the distance between the camera and the specimen to obtain an average speckle size of 64 pixels. Illumination was performed using two Nila LED lights. A calibration plate was used to calibrate the pair of cameras for stereo DIC. Processing of the stereo DIC images was carried out using LaVision DaVIS 8 software. A subset size of 49 x 49 pixels was used with 66% subset overlap. Strain components ε_x and ε_y were obtained from the processed full-field datasets by taking the average of a centrally located area (with a size of ~60% of the overall specimen area), where the strain field was uniform. The standard deviation was also extracted from the DIC data. The electrical strain gauge and DIC measurement are limited to in-plane strain measurement. Therefore to validate

the findings in the through-thickness direction the theoretical values of the strain were determined using classical laminate theory, which enabled an estimation of the through-thickness strain, ε_z. Theoretical calculations of strain were determined using classical laminate theory following the approaches described in [1], and finite element modelling with ABAQUS 6.14. The finite element model was constructed using a C3D8R 8-node linear brick mesh with reduced integration and hourglass control. The model replicated the same geometry, stacking sequence and loading configuration as the experimental tensile tests. Mechanical properties of the composite used in the models was obtained from the manufacturer's materials datasheet. The results are shown in Figure 10 and demonstrate that the proposed new planar optical sensor can decouple the three orthogonal strain components, with good correspondence to the other techniques. The DIC measurement overestimates ε_x. Increasing the load would provide a larger strain value, however, as the optical channel was placed between the tensile grips the load was not taken beyond 1 kN, this minimised grip pressure and so prevented damage to the embedded sensor. Crucially ε_x derived from the optical sensor shows excellent agreement with the theory and the strain gauge. Moreover, ε_z from the optical sensor also shows good correspondence with the theory, demonstrating for the first time an optical sensor can obtain the through-thickness strain.

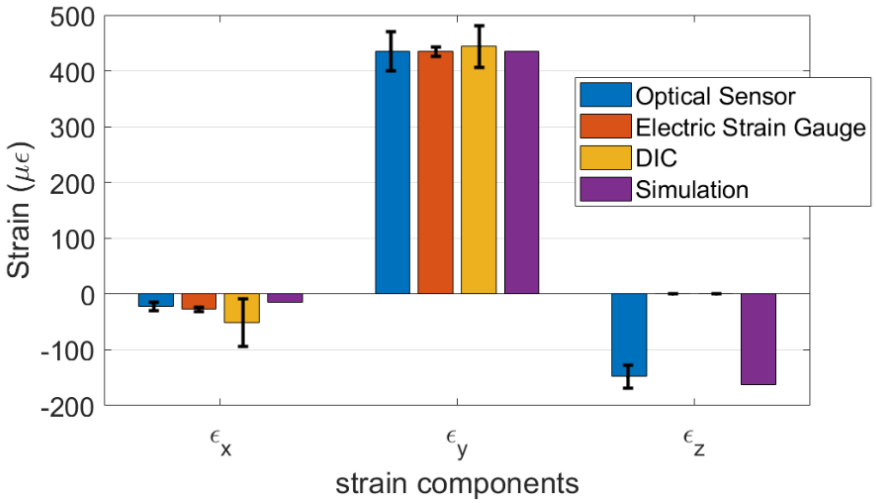

Figure 10 A bar chart comparing the inferred strain response from the optical Bragg sensor compared to that measured through electrical strain gauge (in-plane components) through-thickness component using numerical simulations, for a 1kN load along the y-dimension.

6. Discussion

Decoupling of three orthogonal strain components in CFFP has been demonstrated through birefringence monitoring of planar Bragg gratings. The proof-of-concept demonstration consisted of gratings that have an inherent spectral birefringence, which was less than the spectral bandwidth. This meant that the TE and TM spectral signatures were overlaying each other and thus required individual polarised interrogation. Further developments of the technology could involve tailoring larger inherent birefringence within the planar waveguides, such that the TE and TM gratings are spectrally separated. This would simplify interrogation, through spectral multiplexing, and remove the requirement for polarisation maintaining components.

Deviation in the Pockels coefficients from that of fused silica [21] is assumed due to added dopants during silica glass deposition process. Values of p_{11} = 0.129 and p_{12} = 0.244 provided the closest correlation to the other strain monitoring approaches and are comparable to values for fused silica p_{11} = 0.121 and p_{12} = 0.270 [21] and SMF-28 optical fibre p_{11} = 0.116 and p_{12} = 0.255 respectively (at a

wavelength 1531 nm) [22]. Quantitative investigations into the Pockels coefficients for FHD glass recipes would be useful for future directions in optimised design.

Deviation in local strain and temperature measurements could have also manifested as the proof-of-concept considered two separate sensor chips, placed orthogonally. As these chips were separated by 10's of mm, one would expect small localised variations. From the thermo-optic calibration made (section 5.2), a 1 ^{o}C change in temperature could correspond to a ~0.02 nm spectral discrepancy. Future developments of this technology could feasibly combine the sensor elements upon a single planar optical device, ensuring confined co-location of measurement. The physical length of the Bragg gratings was 12 mm, which could feasibly be reduced to <1 mm, if greater spatial resolutions were desired.

Optical launch into the sensors was achieved through external optical fibre alignment. Currently, this limits the scalability of the technology. Future developments are needed to solve fibre-to-planar coupling within the composite material. In addition to sensor scalability, this could also offer new functionality within composites through utilising more sophisticated integrated optical circuitry. For example, spectral multiplexing and switching which route or re-route an embedded optical sensor network.

7. Conclusion

The work described in the paper provides the first demonstration of an embedded planar optical strain sensor that can measure and decouple through-thickness and in-plane strain components in a laminated composite material. The strain response inferred from the planar sensor was consistent with strain calculations from classical laminate theory and independent strain values measured from foil strain gauges and digital image correlation. To the authors' knowledge, this is the first, potentially scalable demonstration of through-thickness strain monitoring of advanced composites.

The planar optical sensors were observed to have minimal influence on composite structural integritywhen compared to an embedded optical fibre and coupons without an embedded sensor. The influence of the new sensors wasshown to have a negligible mechanical influence after their surface had been roughened or edges tapered.

The planar optical strain sensor is a unique innovation, which potentially enables data-rich information to further complement understanding of a structure's response through embedded sensor networks. The potential application for this work could include long term structural health monitoring, particularly for examining through-thickness strain behaviour caused by delamination, composite damage or impact loading. Potential applications could also further utilise the inherent functionality associated with integrated optics. This includes enabling optical routing of fibre telecommunications through spectral division multiplexing and switching capability within a composite structure.

In the proof of concept, demonstration planar silica circuits were embedded in CRFP. It should be noted that other optical materials including polymers could also be considered in future applications, leveraging different mechanical and optical functionality.

Acknowledgments

The authors thank Hazel Mitchell and Maria Stagno Navarra for their help with data processing and electromechanical testing respectively and James Gates and Paolo Mennea for maintenance of the direct UV writing laser system. The authors are also grateful to Fibrecore for provision of polyimide fibre and GKN Aerospace for provision of CFRP material.

Funding

Higher Education Innovation Funding: University of Southampton Zepler Institute Research Collaboration Stimulus Fund.

References

[1] Y. Li, K. Wang, and Z. Su, "Dispersed sensing networks in nano-engineered polymer composites: From static strain measurement to ultrasonic wave acquisition," *Sensors (Switzerland)*, vol. 18, no. 5, 2018.

[2] W. Obitayo and T. Liu, "A review: Carbon nanotube-based piezoresistive strain sensors," *J. Sensors*, vol. 2012, p. 15, 2012.

[3] M. Kupke, K. Schulte, and R. Schüler, "Non-destructive testing of FRP by d.c. and a.c. electrical methods," *Compos. Sci. Technol.*, vol. 61, no. 6, pp. 837–847, 2001.

[4] M. Sánchez, R. Moriche, S. G. Prolongo, A. R. Marrón, A. Jiménez-Suárez, and A. Ureña, "Evaluation of sensitivity for detecting different failure modes of epoxy matrix composites doped with graphene nanoparticles," *Compos. Struct.*, vol. 225, no. April, p. 111167, 2019.

[5] M. Majumder, T. K. Gangopadhyay, A. K. Chakraborty, K. Dasgupta, and D. K. Bhattacharya, "Fibre Bragg gratings in structural health monitoring-Present status and applications," *Sensors Actuators, A Phys.*, vol. 147, no. 1, pp. 150–164, 2008.

[6] P. Taylor and C. Boller, "Next generation structural health monitoring and its integration into aircraft design Next generation structural health monitoring and its integration," *Int. J. Syst. Sci.*, vol. 31, no. August 2013, pp. 37–41, 2010.

[7] G.Zhou and L.M.Sim, "Damage detection and assessment in fibre-reinforced composite structures with embedded fibre optic sensors-review," *Smart Mater. Struct.*, vol. 11, pp. 925–939, 2002.

[8] X. Zhang *et al.*, "Monitoring the failure forms of a composite laminate system by using panda polarization maintaining fiber Bragg gratings," *Opt. Express*, vol. 27, no. 13, pp. 17571–17580, 2019.

[9] J. Missinne *et al.*, "Bragg-grating-based photonic strain and temperature sensor foils realized using imprinting and operating at very near infrared wavelengths," *Sensors (Switzerland)*, vol. 18, no. 8, pp. 1–14, 2018.

[10] J. Hu, L. Li, H. Lin, P. Zhang, W. Zhou, and Z. Ma, "Flexible integrated photonics: where materials, mechanics and optics meet [Invited]," *Opt. Mater. Express*, vol. 3, no. 9, p. 1313, Aug. 2013.

[11] L. Li *et al.*, "Monolithically integrated stretchable photonics," *Light Sci. Appl.*, vol. 7, no. 2, p. 17138, 2018.

[12] L. Li *et al.*, "A new twist on glass: A brittle material enabling flexible integrated photonics," *Int. J. Appl. Glas. Sci.*, vol. 8, no. 1, pp. 61–68, 2017.

[13] L. Li *et al.*, "Integrated flexible chalcogenide glass photonic devices," *Nat. Photonics*, vol. 8, no. 8, pp. 643–649, 2014.

[14] L. Fan, L. T. Varghese, Y. Xuan, J. Wang, B. Niu, and M. Qi, "Direct fabrication of silicon photonic devices on a flexible platform and its application for strain sensing," *Opt. Express*, vol. 20, no. 18, p. 20564, 2012.

[15] S. Ambran *et al.*, "Fabrication of a Multimode Interference Device in a Low-Loss Flat-Fiber Platform Using Physical Micromachining Technique," *J. Light. Technol.*, vol. 30, no. 17, pp. 2870–2875, 2012.

[16] K. Kalli *et al.*, "Flat fibre and femtosecond laser technology as a novel photonic integration

platform for optofluidic based biosensing devices and lab-on-chip applications: Current results and future perspectives," *Sensors Actuators, B Chem.*, vol. 209, pp. 1030–1040, 2015.
[17] C. Holmes, "Strain tuning of a composite silica-on-silicon direct ultraviolet written planar Bragg grating," *Opt. Eng.*, vol. 49, no. 4, p. 044601, Apr. 2010.
[18] C. Holmes, J. C. Gates, and P. G. R. Smith, "Integrated optical differential pressure transducers achieved using thin buckled silica membranes and direct UV written planar Bragg gratings," *Sensors Actuators A Phys.*, vol. 168, pp. 14–21, Jul. 2011.
[19] Robert G Hunsperger, *Integrated Optics : Theory and Technology*, Sixth Edit. Springer, Springer New York, 2009.
[20] J. S. Sirkis, "Unified approach to phase-strain-temperature models for smart structure interferometric optical fiber sensors: part 1, development," *Opt. Eng.*, vol. 32, no. 4, p. 752, 1993.
[21] D. . Lide, *CRC Handbook of Chemistry and Physics*, 84th ed. CRC Press, 2003.
[22] X. Roselló-Mechó, M. Delgado-Pinar, A. Díez, and M. V. Andrés, "Measurement of Pockels' coefficients and demonstration of the anisotropy of the elasto-optic effect in optical fibers under axial strain," *Opt. Lett.*, vol. 41, no. 13, p. 2934, 2016.
[23] C. Holmes *et al.*, "Direct UV-written planar Bragg grating sensors," *Meas. Sci. Technol.*, vol. 26, no. 11, p. 112001, 2015.